CHEMISTRY OF MATERIALS

pubs.acs.org/cm Article

Tunable Lithium-Ion Transport in Mixed-Halide Argyrodites $Li_{6-x}PS_{5-x}ClBr_x$: An Unusual Compositional Space

Sawankumar V. Patel,[#] Swastika Banerjee,[#] Haoyu Liu, Pengbo Wang, Po-Hsiu Chien, Xuyong Feng, Jue Liu, Shyue Ping Ong,* and Yan-Yan Hu*

Cite This: *Chem. Mater.* 2021, 33, 1435−1443 Read Online

ACCESS | Metrics & More | Article Recommendations | Supporting Information

ABSTRACT: Argyrodites, with fast lithium-ion conduction, are promising for applications in rechargeable solid-state lithium-ion batteries. We report a new compositional space of argyrodite superionic conductors, $Li_{6-x}PS_{5-x}ClBr_x$ [$0 \le x \le 0.8$], with a remarkably high ionic conductivity of 24 mS/cm at 25 °C for $Li_{5.3}PS_{4.3}ClBr_{0.7}$. In addition, the extremely low lithium migration barrier of 0.155 eV makes $Li_{5.3}PS_{4.3}ClBr_{0.7}$ highly promising for low-temperature operation. Average and local structure analyses reveal that bromination ($x > 0$) leads to (i) retention of the parent Li_6PS_5Cl structure for a wide range of x in $Li_{6-x}PS_{5-x}ClBr_x$ ($0 \le x \le 0.7$), (ii) co-occupancy of Cl^-, Br^-, and S^{2-} at 4a/4d sites, and (iii) gradually increased Li^+-ion dynamics, eventually yielding a "liquid-like" Li-sublattice with a flattened energy landscape when x approaches 0.7. In addition, the diversity of anion species and Li-deficiency in halogen-rich $Li_{6-x}PS_{5-x}ClBr_x$ induce hypercoordination and coordination entropy for the Li-sublattice, also leading to enhanced Li^+-ion transport in $Li_{6-x}PS_{5-x}ClBr_x$. This study demonstrates that mixed-anion framework can help stabilize highly conductive structures in a compositional space otherwise unstable with lower anion diversity.

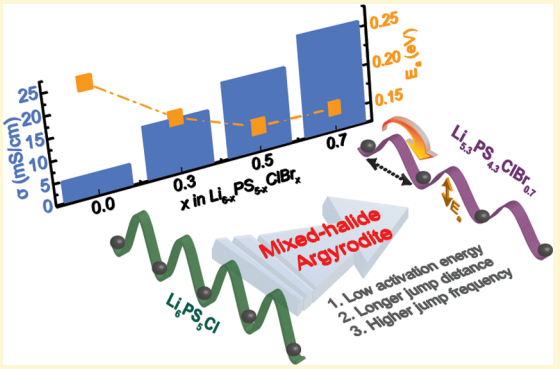

INTRODUCTION

High-performance rechargeable batteries are the leading technology for energy storage. Compared with current rechargeable lithium-ion batteries (LIBs) which employ liquid electrolytes,[1] solid-state batteries (SSBs) using solid electrolytes afford new battery chemistry with enhanced energy and/or power densities, along with improved thermal and electrochemical stability.[2,3] Solid electrolytes with high ionic conductivity and low activation barrier for ion transport are especially crucial for high-power applications of SSBs over a wide range of temperatures.[4]

Recently there has been renewed interest toward the argyrodite family Li_6PS_5X (X = Cl, Br, I), which was first reported in 2008 by Deiseroth et al. The original silver- and copper-based argyrodites[5] adopt two phases, orthorhombic at low temperature and cubic at high temperature. Li_6PS_5X adopts the cubic structure (space group $F\text{-}43m$), in which Li^+ ions occupy crystallographic sites, 24 g and 48 h, and in some cases as recently reported 16e sites.[6] Halide anions occupy the face-centered cubic (FCC) lattice, with PS_4^{3-} tetrahedra filling the octahedral sites (Wyckoff 4b for phosphorus and 16e for sulfur).[7] The rest of sulfur occupies Wyckoff 4d sites, denoted as S_{4d} hereafter. The site exchange between halogen at 4a (0, 0, 0) and sulfur at 4d (0.25, 0.25, 0.75) has been shown to be important for achieving high ionic conductivity.[7−9] Recent studies employed aliovalent substitution of cations to enhance ionic conductivity. For example, substitution of phosphorus with silicon and antimony results in $Li_{6.6}Si_{0.6}Sb_{0.4}S_5I$, with an ionic conductivity of ∼25 mS/cm.[10] Similarly, substitution of phosphorus with germanium yields $Li_{6+x}P_{1-x}Ge_xS_5I$ with an ionic conductivity of 18.4 mS/cm.[8] Although these studies have realized impressive ionic conductivity, narrow electrochemical stability window, and/or high cost for cations such as germanium hinder their practical applications.[11] In addition, cation doping increases conductivity by elevating the prefactor without significantly lowering the activation energy, often resulting in sluggish Li^+-transport at low temperatures.[8,10]

Mixed-anion materials involving multiple species in the anion sublattice open up a new venue for tuning the structures and energy landscape for ion migration.[12−14] Recently, high ionic conductivity of 12 mS/cm with activation energy of 0.29 eV was achieved by varying the anion content, such as in chlorine-rich argyrodite $Li_{5.5}PS_{4.5}Cl_{1.5}$.[15] The enhancement of ionic conductivity was determined to be due to increase in the Cl^-/S^{2-} site disorder. The bond between lithium and anion (S

Received: December 4, 2020
Revised: January 21, 2021
Published: February 3, 2021

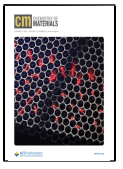

https://dx.doi.org/10.1021/acs.chemmater.0c04650
Chem. Mater. 2021, 33, 1435−1443

and Cl) was weakened by substituting sulfur with chlorine, resulting in a Li-sublattice with high mobility. In addition, Zeier and coworkers have shown that softness of the anion sublattice in Li_6PS_5X (X = Cl, Br, and I) leads to lower activation barrier but also a decreased prefactor for Li^+ conduction.[7]

In this work, we report the discovery of a new compositional space, $Li_{6-x}PS_{5-x}ClBr_x$ ($0 \leq x \leq 0.8$), that yields stable structures with both low activation barriers and significantly increased prefactor for ion migration. Meanwhile, it also provides a platform for examining the effects of Li-vacancies and mixed anionic framework on Li^+ conduction.[16,17] The choice of the anions S^{2-}, Cl^-, and Br^- with subtle differences in size, charge, and bonding patterns gives rise to an argyrodite phase with the highest halogen content ($x = 0.7$) synthesized so far. By combining solid-state NMR and neutron total scattering analysis, the local structural environments of Li^+ ions and anion sublattices are determined. A very high conductivity of 24 mS/cm at 25 °C with a very low activation energy of 0.155 eV has been achieved for the composition of $Li_{5.3}PS_{4.3}ClBr_{0.7}$. DFT and *ab initio* molecular dynamics (AIMD) simulations provide insights into the Li^+ transport mechanisms and reveal a flat energy landscape for anion ordering in the vicinity of the composition $Li_{5.25}PS_{4.25}ClBr_{0.75}$, leading to similar stability for many configurations of varied anion ordering. In turn, the large entropy in anion ordering and Li-anion coordination environments substantially lower barriers for ion transport with enhanced ion mobility and jump steps. The synergistic experimental and computational investigations shed light on the effects of a mixed-anion lattice on active cation conduction in argyrodites and beyond.

EXPERIMENTAL METHODS

Synthesis. The precursor materials, LiCl (>99.9% Sigma-Aldrich), LiBr (>99.9% Sigma-Aldrich), Li_2S (>99.9% Alfa-Aesar), and P_2S_5 (>99.9% Sigma-Aldrich), were weighed based on the stoichiometric ratio and finely ground in a mortar with a pestle, followed by high-energy mechanical milling for 30 min in a zirconia jar with 10 mm zirconia balls. All procedures were conducted under an argon atmosphere in a MBRAUN glovebox. The as-prepared powders were annealed at 300 °C for 12 h and pelletized uniaxially into 6 mm pellets, followed by final sintering between 450 and 550 °C, depending on the $Li_{6-x}PS_{5-x}ClBr_x$ composition, for 12 h under static vacuum.

Solid-State NMR. ^6Li, ^7Li, and ^{31}P magic-angle-spinning (MAS) NMR experiments were performed using a Bruker AVANCE-III 500 spectrometer at Larmor frequencies of 73.6, 194.4, and 202.4 MHz, respectively. The MAS rate was 25 kHz. For ^6Li and ^7Li, single-pulse NMR experiments were performed using $\pi/2$ pulse lengths of 4.75 and 3.35 μs, respectively. The recycle delays were 500 s for ^6Li and 5 s for ^7Li. For ^{31}P, a rotor-synchronized spin-echo sequence was employed with a $\pi/2$ pulse length of 4.2 μs and a recycle delay of 300 s. $^{6,7}Li$ and ^{31}P NMR spectra were calibrated to $LiCl_{(s)}$ at −1.1 ppm and 85% $H_3PO_{4(l)}$ at 0 ppm, respectively. ^{35}Cl and ^{79}Br MAS NMR experiments were performed on an 830 MHz (19.6 T) spectrometer at Larmor frequencies of 81.4 and 208.3 MHz, respectively. ^{79}Br NMR was obtained using the Carr−Purcell−Meiboom−Gill (CPMG) pulse sequence under static conditions with a train of $\pi/2$ pulses of 1 μs and a recycle delay of 1 s. ^{35}Cl NMR was obtained using the rotor-synchronized spin-echo sequence at 16 kHz with a $\pi/2$ pulse length of 2.9 μs and a recycle delay of 20 s. ^{79}Br and ^{35}Cl NMR shifts were calibrated with solid KBr (54.5 ppm) and LiCl (9.93 ppm), respectively. All the NMR spectra were analyzed using the Bruker Topspin Version 3.6.0 software.

Neutron Total Scattering. The room-temperature neutron total scattering on $Li_{6-x}PS_{5-x}ClBr_x$ (x = 0, 0.3, 0.5, 0.7, and 0.8) was performed at the NOMAD beamline (BL-1B) at the Spallation Neutron Source (SNS) at Oak Ridge National Laboratory (ORNL). Powdered (~0.15 g) samples were packed into 3 mm quartz capillaries and sealed with epoxy in a glovebox filled with dry argon. The acquisition time was 1 h for each sample. The background was subtracted from the acquired data followed by normalization against the vanadium rod to generate the total scattering structure factor, $S(Q)$. The normalized $S(Q)$ was then converted to the reduced pair distribution function, $G(r)$, through sine Fourier transformation within a Q (scattering vector) range from 0.3 to 20 $Å^{-1}$ using the IDL codes.[18]

Rietveld Analysis. Rietveld refinement of Bragg diffraction data was carried out using GSAS II software.[19] Neutron diffraction data from all detector banks (2−5 at 2θ angles of 31.0, 65.0, 120.4, and 150.1°, respectively) were refined simultaneously. The parameters were refined in a stepwise manner as described by Kraft et al.[7] Atomic occupancy of the anions including Cl^-, Br^-, and S^{2-} (4a *vs* 4d site) were refined by adding constraints in the atomic displacement (U_{iso}) parameters and setting the sum of occupancy as 1.

PDF Refinement. The analysis of the PDF data was carried out in TOPAS (v6) using a small-box method[20] with a fitting range from 1.8 to 20 Å. Before analysis, the instrumental parameters (Q_{damp} and Q_{broad}) were calibrated using the NIST Si 640e standard sample[21] and then fixed (0.025 and 0.033 $Å^{-2}$) for the following structural refinement. Potential structural models ($F\bar{4}3m$, $Pna2_1$, and Cc) were first constructed from the reported literature[22] and refined against the diffraction data. The obtained atomic coordinates and site occupancy were then set as the starting point for the PDF analysis. From there, a local structure with the Cc space group was employed for the final refinement owing to a low value of R_{wp} (*e.g.*, for Li_6PS_5Cl, the R_{wp} is 34.7% in $F\bar{4}3m$, 20.8% in $Pna2_1$, and 18% in Cc). The occupancy of Li was set to evenly distributed among six sites, whereas Cl, Br, and S at 4d and 4a sites were refined with constraints based on the ideal stoichiometry. The atomic distance was restrained using AI_anti_-bump (Li−Li) or Grs_Interaction (Li−S and Li−Cl) functions.

Electrochemical Measurements. The ionic conductivities of $Li_{6-x}PS_{5-x}ClBr_x$ were determined based on Ac impedance spectroscopy acquired using a Gamry Analyzer Reference 600+ with a frequency range of 1 Hz to 5 MHz. Indium foils were pressed on the surfaces of the pellets as blocking electrodes and the pellets were placed in a custom-built cylindrical cell. Impedance measurements were conducted using the CSZ Microclimate chamber within the temperature range of 20 to 120 °C over frequencies from 5 MHz to 1 Hz with an applied voltage of 10 mV.

Structural Relaxations and Stability Analysis. All density functional theory (DFT) structural optimizations were performed with Perdew−Burke−Ernzerhof (PBE) generalized gradient approximation (GGA)[23] using the projector augmented wave (PAW) pseudopotentials, as implemented in the Vienna Ab initio Simulation Package (VASP).[24,25] The calculation parameters were similar to those used in the materials project (MP),[26,27] such as a plane wave energy cutoff of 520 eV. A dense k-point mesh of 4 × 4 × 4 was used during the structure/energy minimizations of unit cell, which was reduced to 2 × 2 × 2 for 2 × 2 × 2 supercells. All analyses were carried out using Pymatgen and Pymatgen-diffusion packages.[28] The initial structure of Li_6PS_5Cl was obtained from the MP database (id: mp-985592). Substitution of Br at the Cl or S sites of Li_6PS_5Cl were performed with rigorous enumeration to identify stable structures of $Li_{6-x}PS_{5-x}ClBr_x$ ($0 \leq x \leq 0.75$). DFT optimizations were performed on all symmetrically distinct orderings of S/Cl/Br and Li/vacancies to identify the lowest energy structures for $Li_{6-x}PS_{5-x}ClBr_x$. Precomputed energies of all other compositions in the Li−P−S−Cl−Br phase space were obtained from the MP database to find the energy above hull (E_{hull}) and electrochemical stability window.[29,30]

Ab Initio Molecular Dynamics. Lithium ion diffusion was studied using nonspin-polarized AIMD simulations in NVT ensemble at room temperature (300 K) and the temperature range of 500−1200 K with 100 K increment. The same DFT methodology as described for structure optimization has been applied for the AIMD simulations. Supercells maintaining the minimum lattice dimension

https://dx.doi.org/10.1021/acs.chemmater.0c04650
Chem. Mater. 2021, 33, 1435−1443

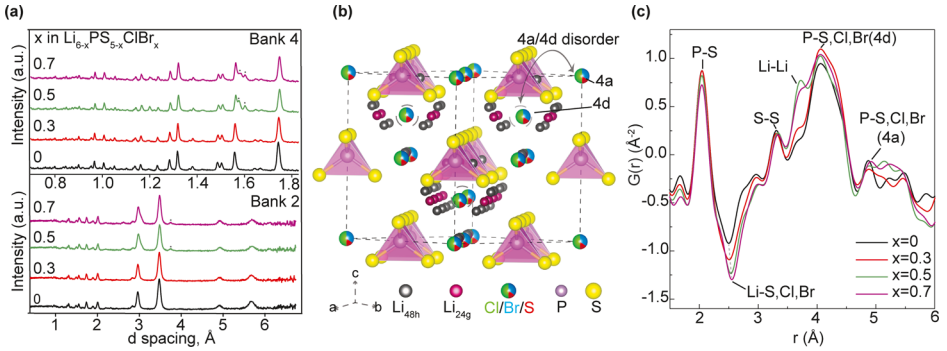

Figure 1. Long- and short-range structural order of mixed-halide argyrodite $Li_{6-x}PS_{5-x}ClBr_x$. (a) Neutron Bragg diffraction patterns of $Li_{6-x}PS_{5-x}ClBr_x$ [$0 \le x \le 0.7$], top displaying the data from bank 4 (small d-spacing) and bottom from bank 2 (large d-spacing). (b) Average crystal structure of argyrodite $Li_{6-x}PS_{5-x}ClBr_x$ (x = 0.7) obtained from refining the Bragg diffraction data as shown in (a), elucidating the occupancy disorder of sulfur, bromine, and chlorine at Wyckoff 4a/4d sites. (c) Neutron pair distribution function (nPDF) of mixed halide argyrodite $Li_{6-x}PS_{5-x}ClBr_x$ [$0 \le x \le 0.7$].

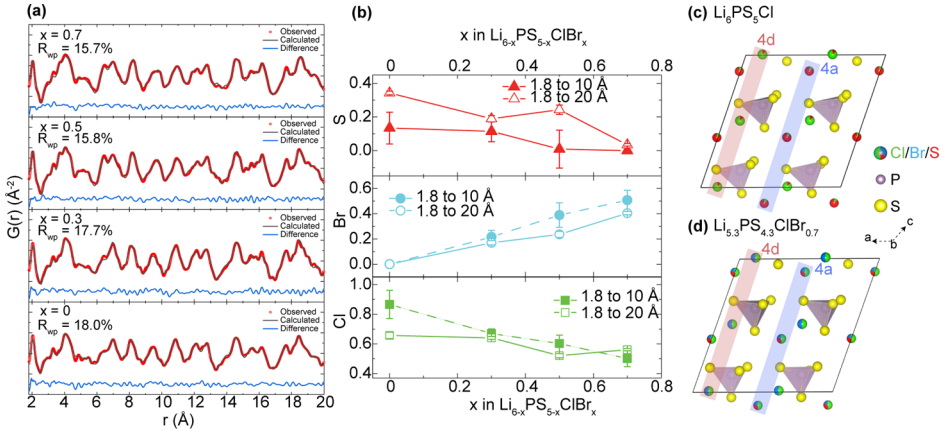

Figure 2. Local structure determination of the mixed-halide argyrodite $Li_{6-x}PS_{5-x}ClBr_x$ with nPDF analysis. (a) Real space refinement of nPDF data on $Li_{6-x}PS_{5-x}ClBr_x$ [x = 0, 0.3, 0.5, and 0.7] using the monoclinic space group cc. (b) S^{2-}, Cl^-, and Br^- site occupancy at 4d in the short range (1.8 to 10 Å), and long range (1.8 to 20 Å). (c,d) Local structures of Li_6PS_5Cl and $Li_{5.3}PS_{4.3}ClBr_{0.7}$ from nPDF refinement.

larger than 10 Å, plane-wave energy cutoff of 280 eV, and a Γ-centered 1 × 1 × 1 k-mesh were used. An automated in-house AIMD workflow program was used for all AIMD calculations with a time step of 2 fs for a total of 200 ps.[31] Diffusivities were computed based on mean square displacement (MSD) at the temperature range between 500 and 1200 K. Subsequently, a converged Arrhenius plot was fitted using the Nernst−Einstein relation to find the activation energy (E_a).

RESULTS

Structural Characterization. To examine the impact of a mixed-anion lattice on the argyrodite structure and Li^+-ion conduction, a series of mixed-halide argyrodites $Li_{6-x}PS_{5-x}ClBr_x$ (x = 0, 0.3, 0.5, and 0.7) are synthesized. For charge balance, Li vacancies are generated upon partial replacement of S^{2-} with Br^-. Neutron diffraction is carried out to determine the average structures of $Li_{6-x}PS_{5-x}ClBr_x$ (x = 0, 0.3, 0.5, 0.7, and 0.8). The diffraction data (Figure 1a) and the corresponding Rietveld refinement (Figures S1 and S2) suggest that the argyrodite structure (space group F-43m) is maintained up to x = 0.7, and further increase in x beyond 0.7 results in the formation of additional impurities (Figure S3). The Rietveld refinement of the diffraction data (Figures S1 and S2) has also shown that with increasing Br content in $Li_{6-x}PS_{5-x}ClBr_x$, a gradual increase in the lattice parameter is found for x < 0.7 but a shrinkage in volume instead for x = 0.7 ($Li_{5.3}PS_{4.3}ClBr_{0.7}$) (Figure S4). The unit cell parameters from refinement are listed in Tables S5 to S8. Along with $Li_{6-x}PS_{5-x}ClBr_x$, a minor (<4%) phase of $LiCl_xBr_{1-x}$ with the rock-salt structure is observed with both Neutron scattering and solid-state NMR. Quantification of the $LiCl_xBr_{1-x}$ phase fraction is documented in Table S9, suggesting x = 0.7 as the limit for considerably phase-pure $Li_{6-x}PS_{5-x}ClBr_x$. In addition, Cl^- redistributes between the Wyckoff 4a and 4d sites, eventually resulting in an equal occupancy, that is, 50% Cl^- at 4a sites and 50% at 4d for x = 0.7 ($Li_{5.3}PS_{4.3}ClBr_{0.7}$). Equal occupancy of S^{2-} and Br^- over 4a and 4d sites is also found in $Li_{5.3}PS_{4.3}ClBr_{0.7}$, suggesting maximum anion disorder or completely random distribution of S^{2-}, Cl^-, and Br^- anions over 4a and 4d sites in $Li_{5.3}PS_{4.3}ClBr_{0.7}$ (Figure 1b). Hence, shrinkage in the overall lattice volume for x = 0.7 is likely a result of anion disorder at Wyckoff 4a/4d sites along with the creation of Li^+-ion vacancies upon increasing Br content in $Li_{6-x}PS_{5-x}ClBr_x$.

For materials with crystallographic site disorder, local or short-range structural order is critical to many functional properties. Hence, the neutron pair distribution function (nPDF), [$G(r)$], is acquired to examine the local structures (Figure 1c). An overlay of the PDF $G(r)$ plots in the short-range (<5 Å) is presented in Figure 1c. The peak around 2 Å represents the P−S pairs in PS_4 tetrahedra, which remains nearly unchanged upon increasing x in $Li_{6-x}PS_{5-x}ClBr_x$, indicating that bromine predominantly exchanges with sulfur

https://dx.doi.org/10.1021/acs.chemmater.0c04650
Chem. Mater. 2021, 33, 1435−1443

at 4a/4d sites and not sulfur in PS_4 tetrahedra. The broadening of the P−$(S/ClBr)_{4d}$ pairs at about 4 Å upon bromination signifies increased variations of local configurations around the PS_4 tetrahedra. This is consistent with the observation from ^{31}P NMR as shown in Figure S7, where an increasing number of the ^{31}P resonances imply a larger diversity of S/Cl/Br occupancy at 4d sites near PS_4 tetrahedra. The negative peak at ∼ 2.5 Å is attributed to Li−(S/Cl/Br) pairs, as lithium has a negative coherent scattering length of −1.9 fm.[32] As shown in Figure 1c, the absolute magnitude of the 2.5-Å peak of the Li−(S/Cl/Br) pairs increases upon bromination, implying perturbation of the Li-(S/Cl) local bonding by Br, which has a larger scattering factor, and thus confirming successful replacement of S^{2-} with Br^- at 4d sites. The 3.6 Å peak from Li−Li pairs in Li_6PS_5Cl (x = 0) shifts toward higher values with increasing x, signifying longer Li−Li distances. This peak is nearly smeared out in $Li_{5.3}PS_{4.3}ClBr_{0.7}$, indicating very disordered Li positions.

The local structure of $Li_{6-x}PS_{5-x}ClBr_x$ is described with the monoclinic symmetry (*Cc*, 9) (Figure 2a) instead of the cubic symmetry (*F*-43*m*, 216) for Li_6PS_5Cl. The decrease in the local symmetry of $Li_{6-X}PS_{5-x}ClBr_x$ implies chemical short-range order (SRO). Indeed, refining the nPDF data over different ranges of the real space (1.8 to 10 *vs* 1.8 to 20 Å) gives rise to slight discrepancy in anion site occupancy. As shown in Figure 2b, slightly higher occupancies of both Cl^- and Br^- at 4d sites (and hence lower occupancies of S^{2-}) are observed when considering a shorter range (1.8 to 10 Å) in the nPDF refinement. The detection of the SRO in the $Li_{6-X}PS_{5-x}ClBr_x$ indicates that the local environments of Li^+ ions can be more heterogeneous than what is described by the average structure, which can affect Li^+ ion migration. The PDF refinement also shows redistribution of anions across the Wyckoff 4a and 4d sites with increasing x in $Li_{6-x}PS_{5-x}ClBr_x$ (Figure 2b). Consistent with the results from the neutron diffraction data, 50% of S^{2-}, Cl^-, and Br^- are populated over the two Wyckoff sites when x = 0.7 ($Li_{5.3}PS_{4.3}ClBr_{0.7}$), suggesting random distribution of these anions between the two sites (Figure 2c,d).

To further investigate the anion reordering in $Li_{6-x}PS_{5-x}ClBr_x$, in particular, Cl^- and Br^- rearrangement, high-field solid-state ^{35}Cl and ^{79}Br NMR spectra are acquired (Figure 3). Two main ^{35}Cl resonances are found, a broad one centered at ∼ −40 ppm and a sharp one at ∼ 9 ppm (Figure 3a), which are attributed to Cl_{4a} and Cl_{4d}, respectively.[9] Semiquantitative analysis of Cl^- site occupancy in $Li_{6-x}PS_{5-x}ClBr_x$ (Figure S6) reveals that Cl^- moves from 4a to 4d sites with increasing x in $Li_{6-x}PS_{5-x}ClBr_x$ and Cl^- occupancy equalizes (50% Cl_{4a} and 50% Cl_{4d}) at x = 0.7 ($Li_{5.3}PS_{4.3}ClBr_{0.7}$), consistent with the PDF and diffraction results. Furthermore, a shoulder gradually grows to the right of the Cl_{4d} resonance as increasing the x value in $Li_{6-x}PS_{5-x}ClBr_x$, suggesting Cl^- positioned off the center of 4d sites. ^{79}Br NMR of $Li_{6-x}PS_{5-x}ClBr_x$ (Figure 3b) also reveals mixed site occupancy of Br^- over Wyckoff 4a and 4d sites, with Br_{4d} increases with x and $Li_{5.3}PS_{4.3}ClBr_{0.7}$ showing 50% of Br^- at 4d sites (Figure S6). Overall, both ^{35}Cl and ^{79}Br NMR results suggest again random distribution of S^{2-}, Cl^-, and Br^- among the 4a/4d sites in $Li_{5.3}PS_{4.3}ClBr_{0.7}$. The parameters used to fit the ^{35}Cl and ^{79}Br spectra are specified in Tables S2 and S3, respectively.

To understand the effects of Br content on anion disorder, DFT calculations are carried out to determine the energy for

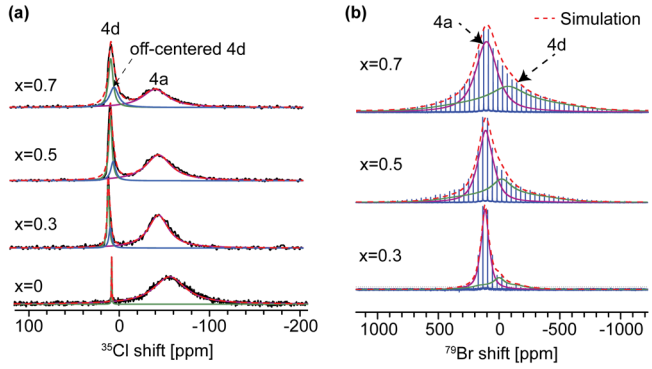

Figure 3. Cl^- and Br^- anion ordering in $Li_{6-x}PS_{5-x}ClBr_x$ revealed by NMR. (a) ^{35}Cl NMR of $Li_{6-x}PS_{5-x}ClBr_x$ [$0 \le x \le 0.7$] with two resonances from Cl located at Wyckoff 4a and 4d sites, respectively; (b) ^{79}Br CPMG NMR and simulation of $Li_{6-x}PS_{5-x}ClBr_x$ [x = 0.3, 0.5, and 0.7] with two resonances from Br located at Wyckoff 4a and 4d sites, respectively.

anion swapping. As shown in Figure 4, the energy penalty for Cl to exchange positions with *S*, E_{swap}, is highly positive (>40 meV per swapped anion) for stoichiometric Li_6PS_5Cl. As Br is doped into the system, E_{swap} decreases to a small negative value (1−3 meV per swapped anion pair). This indicates that Br doping is likely to result in anion disordering, with Br/S/Cl occupying both 4a and 4d sites. It is worth noting that the DFT analyses helps in understanding the tendency for static disorder. However, at operating conditions, many ion conductors including argyrodites exhibit significant dynamic disorder along with the static disorder.[33]

To investigate the effects of anion composition and disorder on Li^+ ion dynamics in $Li_{6-x}PS_{5-x}ClBr_x$, NMR spectroscopy and relaxometry are employed. Figure 5a displays the ^6Li NMR spectra of $Li_{6-x}PS_{5-x}ClBr_x$ (x = 0, 0.3, 0.5, and 0.7). Although Li^+ ions are reported to occupy multiple crystallographic sites such as 24g and 48h, fast Li^+ ion migration across these sites causes coalescence of multiple resonances; thus, the $^6Li_{24g}$ and $^6Li_{48h}$ resonances are not well resolved, even for Li_6PS_5Cl. Diversifying the anion sublattice often results in reduced symmetry of Li local environments and thus, broadening of ^6Li NMR resonances.[34] However, in the case of $Li_6PS_5Cl_{1-x}Br_x$ (x > 0), no significant broadening is observed, instead slight narrowing of the peak width is seen (Figure 5a), suggesting increased Li^+ ion dynamics that yields an average of all asymmetric environments and further coalescence. To more quantitatively evaluate the changes in Li^+-ion dynamics, ^7Li spin−lattice (T_1) relaxation time measurements have been carried out (Table S4). T_1 refers to the time required for the ensemble of spins to recover from nonequilibrium to the equilibrium state, which is primarily driven by fluctuations of local magnetic fields due to motions. The quadrupolar coupling constant of ^7Li is often small; hence, the dipolar coupling interaction is the major driving force of the relaxation process.[35] Bloembergen, Purcell, and Pound developed the BPP model, explaining the correlation time τ_c (mean resident time for nuclear spin at one site before migrating to another site) as an indicator of ion mobility.[36] The correlation of T_1 and τ_c is described in eq 1, where γ is the gyromagnetic ratio, μ_o is the vacuum permeability, $\hbar$ is the reduced Planck constant, r_o is the interatomic distance, and ω_o is the Larmor frequency.[34] Frequency- and temperature-dependent NMR spin relaxation rate measurements on Li_6PS_5Br and Li_6PS_5Cl

https://dx.doi.org/10.1021/acs.chemmater.0c04650
Chem. Mater. 2021, 33, 1435−1443

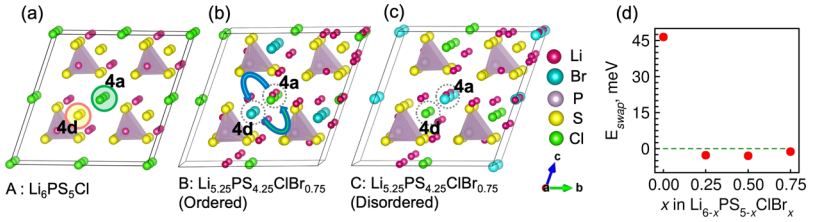

Figure 4. Probability of anion exchange in $Li_{6-x}PS_{5-x}ClBr_x$. DFT-optimized structures of (a) Li_6PS_5Cl with Cl at 4a and S at 4d sites. (b) $Li_{5.25}PS_{4.25}ClBr_{0.75}$ with Cl at 4a and S/Br at 4d site, and (c) Cl/S/Br at both 4a and 4d sites. (d) Variation of the anion swapping energy E_{swap} with Br content (x). E_{swap} is the energy difference between the structures shown in (b) and (c) divided by the number of anions exchanged. The lowest energy ordering is used in all cases. E_{swap} is an estimate of the likelihood that Cl at the 4a sites and S/Br at the 4d sites can exchange positions. The lower the E_{swap}, the lower the energy penalty for anion exchange to take place.

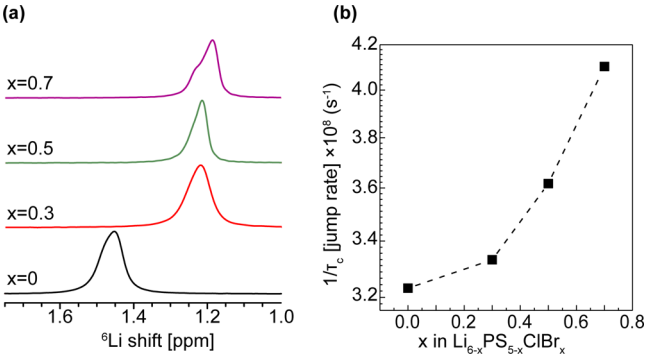

Figure 5. Lithium redistribution and Li^+-ion dynamics in $Li_{6-x}PS_{5-x}ClBr_x$ (x = 0, 0.3, 0.5, and 0.7). (a) ^6Li NMR spectra. (b) Estimated $1/\tau_c$ [jump rate] of $Li_{6-x}PS_{5-x}ClBr_x$ [$0 \le x \le 0.7$] based on ^7Li T_1 relaxation measurements.

have shown that Li^+ ion motion in these argyrodite materials lies in the fast motion (liquid) regime, where $\omega_o\tau_c \ll 1$; therefore, eq 1 can be simplified into eq 2, which reveals that long T_1 relaxation time in this system correlates with short τ_c and thus the fast jump rate ($1/\tau_c$) of Li^+ ions.[37] Figure 5b shows the jump rates $1/\tau_c$ estimated from room-temperature ^7Li T_1 relaxation times of $Li_{6-x}PS_{5-x}ClBr_x$ based on eq 2. Interatomic distance r_o was determined by taking the average Li−Li distance from PDF refinements. The jump rate slightly increases with x in $Li_{6-x}PS_{5-x}ClBr_x$. The attempt frequency of jumps ($1/\tau_o$) was calculated from the jump rate $1/\tau_c$ (Table S4), which decreases with x in $Li_{6-x}PS_{5-x}ClBr_x$. The attempt frequency corresponds to the rate of both the successful and unsuccessful jumps that lead to long-range ion diffusion, whereas the jump rate corresponds to the rate of successful jumps.[38]

$$\left(\frac{1}{T_1}\right) = \frac{3\mu_o^2\gamma^4\hbar^2}{10r_0^6}\left[\frac{\tau_c}{1+(\omega_o\tau_c)^2} + \frac{4\tau_c}{1+4(\omega_o\tau_c)^2}\right] \quad (1)$$

$$\left(\frac{1}{T_1}\right) = \frac{3\mu_o^2\gamma^4\hbar^2}{2r_0^6}\tau_c \quad (2)$$

Enhanced Ionic Conductivity and Low Activation Energy. We have shown that diversifying the anion sublattice has stabilized highly Li-deficient compositions, such as $Li_{5.3}PS_{4.3}ClBr_{0.7}$, created a very flat energy landscape, allowing for completely random distribution of anions (S, Cl, and Br) over 4a/4d sites and enhanced Li^+-ion mobility in a "liquid-like" Li-sublattice. It is expected that all these changes will have an impact on Li ionic conductivity of $Li_{6-x}PS_{5-x}ClBr_x$, which is determined with electrochemical impedance spectroscopy (Figure 6a). As is shown in Figure 6b, the conductivity increases with x in $Li_{6-x}PS_{5-x}ClBr_x$ and peaks at 24 mS/cm at 25 °C for x = 0.7 ($Li_{5.3}PS_{4.3}ClBr_{0.7}$). Further increase in x beyond 0.7 reduces the conductivity due to the formation of additional impurities (Figure S3). The activation energy E_a for ion transport in $Li_{6-x}PS_{5-x}ClBr_x$ is determined by measuring temperature-dependent ionic conductivity (σ) (Figure 6c). E_a is extracted based on eq 3, and the values are listed in Figure 6c.[39] $Li_{5.3}PS_{4.3}ClBr_{0.7}$ exhibits the least activation barrier of 0.155 eV. To place the performance of this material in the context of the most conductive superionic Li^+-ion conductors reported so far, a detailed comparison is presented in Table 1, revealing that $Li_{5.3}PS_{4.3}ClBr_{0.7}$ exhibits the lowest activation energy with the nearly highest ionic conductivity.

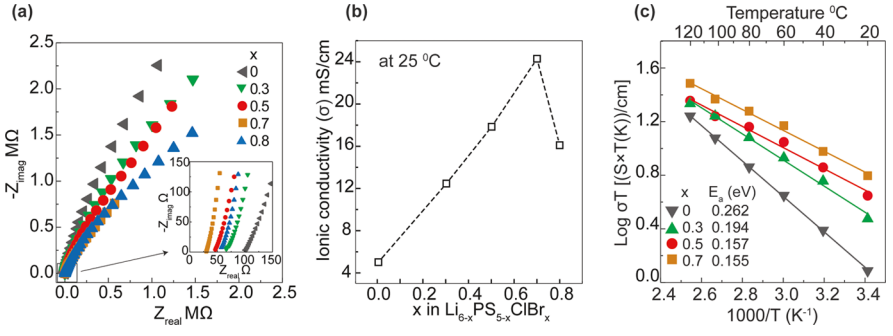

Figure 6. Ionic conductivity and activation energy measurements of mixed-halide argyrodite $Li_{6-x}PS_{5-x}ClBr_x$. (a) Electrochemical AC impedance spectra measured at 20 °C; inset shows the enlarged high-frequency region. (b) Ionic conductivity at 25 °C extrapolated from the Arrhenius plot. (c) Arrhenius plot of ionic conductivity *vs* temperature, and the corresponding activation energy values for each composition.

https://dx.doi.org/10.1021/acs.chemmater.0c04650
Chem. Mater. 2021, 33, 1435−1443

$$\sigma = \frac{\sigma_0}{T} \times e^{(-E_a/k_B T)} \quad (3)$$

Table 1. Comparison of Experimentally Determined Ionic Conductivity and Activation Energy Values of Most Highly Conductive Li^+-Ion Conductors from EIS

solid electrolyte	ionic conductivity (σ) ms/cm (EIS)	activation energy eV (EIS)	reference
$Li_{5.3}PS_{4.3}ClBr_{0.7}$	24	0.155	this work
$Li_{5.5}PS_{4.5}ClBr_{0.5}$	17	0.157	this work
$Li_{6.6}Si_{0.6}Sb_{0.4}S_5I$	24	0.250	(Nazar et al.)[10]
$Li_{6.6}P_{0.4}Ge_{0.6}S_5I$	18	0.250	(Zeier et al.)[8]
$Li_{9.54}Si_{1.74}P_{1.44}S_{11.7}Cl_{0.3}$	25	0.238	(Kanno et al.)[12]
$Li_{10}GeP_2S_{12}$	12	0.269	(Kanno et al.)[12]

Diffusion Mechanism. To further understand the favorable Li^+-ion conduction in $Li_{6-x}PS_{5-x}ClBr_x$, diffusion characteristics have been analyzed using AIMD simulations (Figure 7a, Table S1). In agreement with the experimental

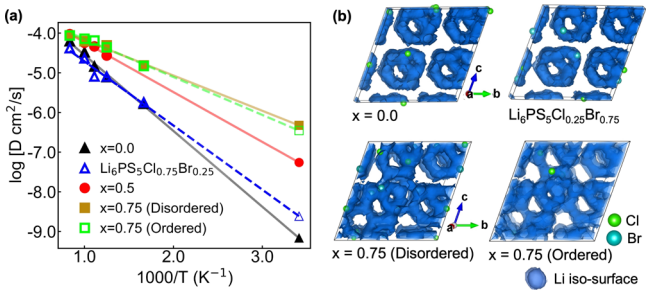

Figure 7. Li diffusion analyzed using AIMD simulations. (a) Calculated Li diffusivity (D) at various temperatures (T) for $Li_{6-x}PS_{5-x}ClBr_x$ [x = 0, 0.50, and 0.75]; corresponding Li-migration barriers (in eV) are given in Table S1. Dashed lines represent the result of the two computationally experimented cases: (1) Li-diffusion characteristics of $Li_6PS_5Cl_{1-x}Br_x$ which is without Li vacancies but with Cl/Br mixing and (2) ordered $Li_{5.25}PS_{4.25}ClBr_{0.75}$. (b) Isosurfaces of the Li-ion probability densities are plotted at isovalues $P_0/8$, in which P_0 is defined as the mean value of the density for $Li_6PS_5Cl_{0.25}Br_{0.75}$ and $Li_{6-x}PS_{5-x}ClBr_x$ [x = 0.0, 0.75] with and without 4a/4d anion ordering.

results, an enhanced conductivity of 30−56 mS cm^{-1} is computationally estimated for $Li_{5.25}PS_{4.25}ClBr_{0.75}$ compared to 0.33−0.65 mS cm^{-1} for Li_6PS_5Cl. While improved conductivity has been observed earlier in Lithium excess (n_{Li} > 6) argyrodites,[8,10] this is the first observed instance of Li-deficient (n_{Li} < 6) halogen-rich argyrodite framework accompanied by a significant reduction in Li^+ ion migration barrier, E_a = 0.180 ± 0.03 eV for x = 0.75 *versus* 0.349 ± 0.02 eV for x = 0. To understand the origin of this decreased activation energy E_a for Li^+ ion transport in $Li_{6-x}PS_{5-x}ClBr_x$, we have analyzed the distribution probability for Li at 600 K in Li_6PS_5Cl and $Li_{5.25}PS_{4.25}ClBr_{0.75}$, as shown in Figure 7b. Li_6PS_5Cl exhibits restricted "cage-like" lithium diffusion with no intercage jump between the pairs of 48h sites, thus suggesting only short-range Li^+ ion migration and explaining the poor macroscopic Li^+ ion conduction in pristine Li_6PS_5Cl. In contrast, $Li_{5.25}PS_{4.25}ClBr_{0.75}$ exhibits interconnected Li domains that form diffusion channels, regardless of the ordering of anions.

The two structural configurations of $Li_{5.25}PS_{4.25}ClBr_{0.75}$: ordered and disordered as shown in Figure 4b,c, respectively, are examined with MD simulations. Both the configurations exhibit comparable Li-migration barriers (0.180 ± 0.03 eV; Figure 7a) and similar long-range Li diffusion paths (Figure 7b). This computational experiment highlights the limitation to directly correlate the degrees of anion site disorder with enhanced lithium conductivity. Thus, $Li_{5.25}PS_{4.25}ClBr_{0.75}$ represents a compositional space where the arrangement of anions does not induce significant changes in the already flattened energy landscape, which in turn has negligible effect on the Li-diffusivity (Figure 7).

To further understand the Li environments within $Li_{6-x}PS_{5-x}ClBr_x$ that attribute to faster Li-transport, the MD-averaged Li−Li correlation function at room temperature is shown in Figure 8a. The peak at ∼ 3.6 Å for Li_6PS_5Cl

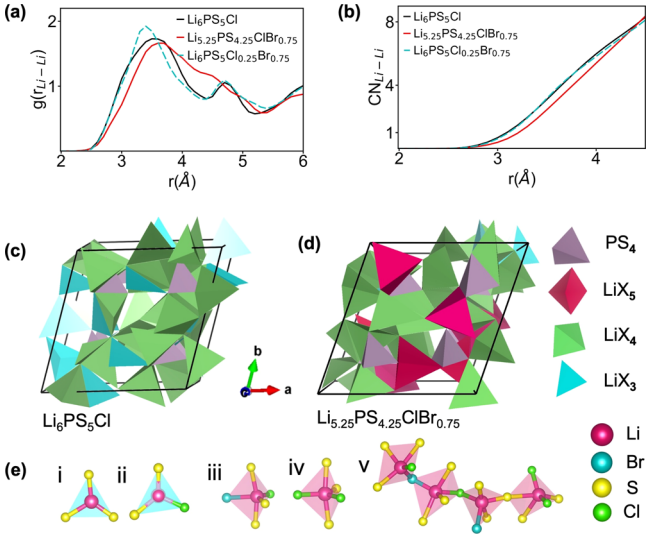

Figure 8. (a) Li−Li pair distribution function from the 200 ps MD trajectory at room temperature (300 K) for Li_6PS_5Cl, $Li_6PS_5Cl_{0.25}Br_{0.75}$, and $Li_{5.25}PS_{4.25}ClBr_{0.75}$. (b) Number of neighboring Li (CN_{Li-Li}) *vs* Li−Li distance for $Li_{6-x}PS_{5-x}ClBr_x$ (x = 0, 0.75) and $Li_6PS_5Cl_{0.25}Br_{0.75}$. (c) Li_6PS_5Cl exhibits LiX_n-polyhedra with $n \leq 4$ (green polyhedra). (d) Hypercoordination of Li in $Li_{5.25}PS4_{.25}ClBr_{0.75}$ leads to LiX_n-polyhedra (X = S, Cl, Br) with n > 4 (magenta polyhedra). (e) Distinct local environments of Li in $Li_{5.25}PS_{4.25}ClBr_{0.75}$, exhibiting coordination number low (n = 3) or high (n = 5) besides the LiX_4-tetrahedra.

significantly broadens for $Li_{5.25}PS_{4.25}ClBr_{0.75}$ (see Figure 8a). Thus, the long-range order for Li-ion distribution is disrupted upon bromination, leading to more liquid-like behavior for the Li-sublattice that hints for high Li^+-ion conductivity. In addition, MD-derived PDF analysis reveals that the Li−S coordination sphere has relatively fewer number of Li compared to Li−X (X = Cl, Br) coordination, leading to a molten Li-sublattice surrounding halogens (Figure S5). Neutron PDF analysis also reveals the weakening of the Li-anion local coordination after increasing the halogen content, x (Figure 1c), signifying more labile Li in $Li_{6-x}PS_{5-x}ClBr_x$ (x > 0). While integrating the number of Li up to ∼4.5 Å (Figure 8b), we find a more dispersed Li^+ ion distribution in $Li_{5.25}PS_{4.25}ClBr_{0.75}$ compared to Li_6PS_5Cl. Dispersed Li^+ ions not only stabilize the system by lowering Coulombic repulsion but also lead to a longer Li-jump distance.

https://dx.doi.org/10.1021/acs.chemmater.0c04650
Chem. Mater. 2021, 33, 1435−1443

A distinct bonding feature in $Li_{5.25}PS_{4.25}ClBr_{0.75}$ is the hypercoordinated Li exhibiting LiX_n-polyhedra (X = S, Cl, Br) with $n > 4$ (Figure 8d), attributed to the lowering of Li/X ratio in halogen-rich Li-deficient argyrodites, while Li_6PS_5Cl exhibits LiX_n-polyhedra restricted with $n \leq 4$ (Figure 8c). In addition to hypercoordination, Li adopts multiple environments in $Li_{5.25}PS_{4.25}ClBr_{0.75}$, namely, angular, trigonal plane, triangular non-coplanar, T-shaped, tetrahedron, square plane, and trigonal bipyramid (selected examples shown in Figure 8e). The wide range of Li-coordination environments prevails for both the ordered and disordered configurations of $Li_{5.25}PS_{4.25}ClBr_{0.75}$. Thus, increasing the anion-diversity and Li-vacancy, to a certain degree, diversifies the Li chemical environments, leading to coordination entropy. Diversity in Li−X coordination environments for $Li_{5.25}PS_{4.25}ClBr_{0.75}$ facilitates Li diffusion due to no net change in Li−X coordination numbers during Li-hopping.

Anion composition, anion disorder, and Li deficiency in $Li_{6-x}PS_{5-x}ClBr_x$ can all affect ion conduction. In order to evaluate their respective contributions, we have compared experimental results on $Li_{5.5}PS_{4.5}ClBr_{0.5}$, $Li_6PS_5Cl_{0.5}Br_{0.5}$,[35] $Li_{5.5}PS_{4.5}Cl_{1.5}$,[15] $Li_{5.5}PS_{4.5}Br_{1.5}$,[34] and Li_6PS_5Cl (Table 2). The comparison between $Li_{5.5}PS_{4.5}Cl_{1.5}$, and Li_6PS_5Cl suggests that $Cl^- > S^{2-}$ substitution and induced Li deficiency enhance the ionic conductivity (12 mS/cm *vs* 2 mS/cm) by increasing the prefactor but does not change the activation energy significantly (0.29 eV *vs* 0.32 eV). The comparison between the $Li_{5.5}PS_{4.5}Br_{1.5}$ and $Li_{5.5}PS_5Cl_{1.5}$ pair indicates that higher Br content results in significantly lower activation energy (0.18 eV *vs* 0.29 eV) but smaller prefactor (11 mS/cm *vs* 12 mS/cm). Therefore, $Li_{6-x}PS_5Cl_{1-x}Br_x$ ($x > 0$) represents a special compositional space where Li-deficiency mainly attributes to increasing the prefactor, while Br softens the anion lattice and significantly reduces the activation barrier. Uniquely in this compositional space, the energy landscape is flattened (Figure 4b) and maximum anion disorder is achieved; both contribute to further increase of the prefactor and the reduction of activation barrier. This synergistic effect can be qualitatively evaluated by comparing $Li_{5.5}PS_{4.5}ClBr_{0.5}$ and $Li_{5.5}PS_{4.5}Br_{1.5}$: both have the same Li-deficiency and S content, despite that $Li_{5.5}PS_{4.5}ClBr_{0.5}$ has much lower Br content, and $Li_{5.5}PS_{4.5}ClBr_{0.5}$ exhibits higher ionic conductivity (17 mS/cm *vs* 11 mS/cm) and lower activation barrier (0.16 eV *vs* 0.18 eV).

Table 2. Comparison of Experimentally Determined Ionic Conductivity and Activation Energy of Various Mixed-Halide Argyrodite Solid Electrolytes from EIS

formula	E_a (eV)	ionic conductivity (σ) (mS/cm)	reference
Li_6PS_5Cl	0.32	2	[Wilkening et al.][35]
$Li_{5.5}PS_{4.5}Cl_{1.5}$	0.29	12	[Nazar et al.][15]
$Li_6PS_5Cl_{0.5}Br_{0.5}$	0.30	3	[Wilkening et al.][35]
$Li_{5.5}PS_{4.5}ClBr_{0.5}$	0.16	17	[this work]
$Li_{5.5}PS_{4.5}Br_{1.5}$	0.18	11	[Hu et al.][34]

CONCLUSIONS

In summary, we have investigated the compositional space $Li_{6-x}PS_{5-x}ClBr_x$ [$0 \leq x \leq 0.8$] with a combined experimental and computational approach and highlighted the underlying principles of anion diversity to achieve halogen-rich argyrodite framework with threefold benefits of good phase stability, high Li-conductivity, and low activation energy. $Li_{6-x}PS_{5-x}ClBr_x$ exhibits mixed occupancy of S, Cl, and Br at Wycoff 4a/4d sites, as characterized by ^{35}Cl and ^{79}Br NMR, as well as neutron diffraction and pair distribution function. $Li_{6-x}PS_{5-x}ClBr_x$ ($x > 0$) also exhibits a "liquid-like" lithium sublattice. The highest room-temperature Li^+-ion conductivity of 24 mS/cm associated with the lowest activation barrier of 0.155 eV is found in $Li_{5.3}PS_{4.3}ClBr_{0.7}$, promising for low-temperature operation. Multiple anionic species in Li-deficient halogen-rich $Li_{6-x}PS_{5-x}ClBr_x$ diversify the Li-chemical environments in terms of the coordination number and the shape of the coordination shell. At a high halogen content limit of $x = 0.75$, coordination entropy appears irrespective of the anion site ordering. Such Li-coordination entropy gives rise to the fast Li^+-ion transport due to no net change in Li−X coordination numbers during the hopping process. The experimentally achieved high-performance properties combined with computational insights will inspire new strategies for the design of novel solid electrolytes.

ASSOCIATED CONTENT

Supporting Information

The Supporting Information is available free of charge at https://pubs.acs.org/doi/10.1021/acs.chemmater.0c04650.

Structural information obtained from Rietveld refinement analysis of neutron diffraction data, ^{31}P NMR spectra and the quantification of ^{35}Cl and ^{79}Br NMR results, and possible configurations of mixed-halide structures (PDF)

AUTHOR INFORMATION

Corresponding Authors

Yan-Yan Hu − *Department of Chemistry and Biochemistry, Florida State University, Tallahassee, Florida 32306, United States; Center of Interdisciplinary Magnetic Resonance, National High Magnetic Field Laboratory, Tallahassee, Florida 32310, United States;* orcid.org/0000-0003-0677-5897; Email: yhu@fsu.edu

Shyue Ping Ong − *Department of NanoEngineering, University of California San Diego, San Diego, California 92093-0448, United States;* orcid.org/0000-0001-5726-2587; Email: ongsp@eng.ucsd.edu

Authors

Sawankumar V. Patel − *Department of Chemistry and Biochemistry, Florida State University, Tallahassee, Florida 32306, United States;* orcid.org/0000-0002-5293-9330

Swastika Banerjee − *Department of NanoEngineering, University of California San Diego, San Diego, California 92093-0448, United States;* orcid.org/0000-0001-8202-4628

Haoyu Liu − *Department of Chemistry and Biochemistry, Florida State University, Tallahassee, Florida 32306, United States*

Pengbo Wang − *Department of Chemistry and Biochemistry, Florida State University, Tallahassee, Florida 32306, United States*

Po-Hsiu Chien − *Neutron Scattering Division, Oak Ridge National Laboratory, Oak Ridge, Tennessee 37831, United States;* orcid.org/0000-0002-1607-1271

https://dx.doi.org/10.1021/acs.chemmater.0c04650
Chem. Mater. 2021, 33, 1435−1443

Xuyong Feng − *Department of Chemistry and Biochemistry, Florida State University, Tallahassee, Florida 32306, United States*

Jue Liu − *Neutron Scattering Division, Oak Ridge National Laboratory, Oak Ridge, Tennessee 37831, United States;* orcid.org/0000-0002-4453-910X

Complete contact information is available at: https://pubs.acs.org/10.1021/acs.chemmater.0c04650

Author Contributions

#S.V.P. and S.B. authors contributed equally

Notes

The authors declare no competing financial interest.

■ ACKNOWLEDGMENTS

The authors acknowledge the support from the National Science Foundation under grant no. DMR-1847038. The collaboration was facilitated by the Scialog Award #26319 from Research Corporation for Science Advancement. All solid-state NMR experiments were performed at the National High Magnetic Field Laboratory. The National High Magnetic Field Laboratory is supported by National Science Foundation through NSF/DMR-1644779 and the State of Florida. A portion of this research used resources at the Spallation Neutron Source, a DOE Office of Science User Facility operated by the Oak Ridge National Laboratory. The computational studies were supported by the UCI MRSEC program, Prime Sponsor (NSF) award number DMR-2011967. Computing resources were performed using the Extreme Science and Engineering Discovery Environment (XSEDE), which is supported by the National Science Foundation grant ACI-1053575. Software development and data resources were provided by the Materials Project, funded by the U.S. Department of Energy, Office of Science, Office of Basic Energy Sciences, Materials Sciences and Engineering Division under contract no. DE-AC02-05-CH11231: Materials Project program KC23MP.

■ ABBREVIATIONS

NMR,	nuclear magnetic resonance
MAS,	magic-angle spinning
nPDF,	neutron pair distribution function
EIS,	electrochemical impedance spectroscopy
XRD,	X-ray diffraction
SRO,	short-range order
QCPMG,	quadrupolar Carr−Purcell−Meiboom−Gil
DFT,	density functional theory
AIMD,	Ab initio molecular dynamics.

■ REFERENCES

(1) Kerman, K.; Luntz, A.; Viswanathan, V.; Chiang, Y.-M.; Chen, Z. Review—Practical Challenges Hindering the Development of Solid State Li Ion Batteries. *J. Electrochem. Soc.* **2017**, *164*, A1731−A1744.

(2) Gür, T. M. Review of Electrical Energy Storage Technologies, Materials and Systems: Challenges and Prospects for Large-Scale Grid Storage. *Energy Environ. Sci.* **2018**, *11*, 2696−2767.

(3) Badwal, S. P. S.; Giddey, S. S.; Munnings, C.; Bhatt, A. I.; Hollenkamp, A. F. Emerging Electrochemical Energy Conversion and Storage Technologies. *Front. Chem.* **2014**, *2*, 79.

(4) Chen, R.; Qu, W.; Guo, X.; Li, L.; Wu, F. The Pursuit of Solid-State Electrolytes for Lithium Batteries: From Comprehensive Insight to Emerging Horizons. *Mater. Horiz.* **2016**, *3*, 487−516.

(5) Deiseroth, H.-J.; Kong, S.-T.; Eckert, H.; Vannahme, J.; Reiner, C.; Zaiß, T.; Schlosser, M. Li_6PS_5X: A Class of Crystalline Li-Rich Solids With an Unusually High Li+ Mobility. *Angew. Chem., Int. Ed.* **2008**, *47*, 755−758.

(6) Huang, W.; Cheng, L.; Hori, S.; Suzuki, K.; Yonemura, M.; Hirayama, M.; Kanno, R. Ionic Conduction Mechanism of a Lithium Superionic Argyrodite in the Li−Al−Si−S−O System. *Adv. Mater.* **2020**, *1*, 334−340.

(7) Kraft, M. A.; Culver, S. P.; Calderon, M.; Böcher, F.; Krauskopf, T.; Senyshyn, A.; Dietrich, C.; Zevalkink, A.; Janek, J.; Zeier, W. G. Influence of Lattice Polarizability on the Ionic Conductivity in the Lithium Superionic Argyrodites Li_6PS_5X (X = Cl, Br, I). *J. Am. Chem. Soc.* **2017**, *139*, 10909−10918.

(8) Kraft, M. A.; Ohno, S.; Zinkevich, T.; Koerver, R.; Culver, S. P.; Fuchs, T.; Senyshyn, A.; Indris, S.; Morgan, B. J.; Zeier, W. G. Inducing High Ionic Conductivity in the Lithium Superionic Argyrodites $Li_{6+x}P_{1-X}Ge_xS_5I$ for All-Solid-State Batteries. *J. Am. Chem. Soc.* **2018**, *140*, 16330−16339.

(9) Feng, X.; Chien, P.-H.; Wang, Y.; Patel, S.; Wang, P.; Liu, H.; Immediato-Scuotto, M.; Hu, Y.-Y. Enhanced Ion Conduction by Enforcing Structural Disorder in Li-Deficient Argyrodites $Li_{6-x}PS_{5-x}Cl_{1+x}$. *Energy Storage Mater.* **2020**, *30*, 67−73.

(10) Zhou, L.; Assoud, A.; Zhang, Q.; Wu, X.; Nazar, L. F. New Family of Argyrodite Thioantimonate Lithium Superionic Conductors. *J. Am. Chem. Soc.* **2019**, *141*, 19002−19013.

(11) Chen, H. M.; Maohua, C.; Adams, S. Stability and Ionic Mobility in Argyrodite-Related Lithium-Ion Solid Electrolytes. *Phys. Chem. Chem. Phys.* **2015**, *17*, 16494−16506.

(12) Kato, Y.; Hori, S.; Saito, T.; Suzuki, K.; Hirayama, M.; Mitsui, A.; Yonemura, M.; Iba, H.; Kanno, R. High-Power All-Solid-State Batteries Using Sulfide Superionic Conductors. *Nat. Energy* **2016**, *1*, 16030.

(13) Kim, K.-H.; Martin, S. W. Structures and Properties of Oxygen-Substituted $Li_{10}SiP_2S_{12-X}O_x$ Solid-State Electrolytes. *Chem. Mater.* **2019**, *31*, 3984−3991.

(14) Banerjee, S.; Zhang, X.; Wang, L.-W. Motif-Based Design of an Oxysulfide Class of Lithium Superionic Conductors: Toward Improved Stability and Record-High Li-Ion Conductivity. *Chem. Mater.* **2019**, *31*, 7265−7276.

(15) Adeli, P.; Bazak, J. D.; Park, K. H.; Kochetkov, I.; Huq, A.; Goward, G. R.; Nazar, L. F. Boosting Solid-State Diffusivity and Conductivity in Lithium Superionic Argyrodites by Halide Substitution. *Angew. Chem., Int. Ed.* **2019**, *58*, 8681−8686.

(16) Kageyama, H.; Hayashi, K.; Maeda, K.; Attfield, J. P.; Hiroi, Z.; Rondinelli, J. M.; Poeppelmeier, K. R. Expanding Frontiers in Materials Chemistry and Physics with Multiple Anions. *Nat. Commun.* **2018**, *9*, 772.

(17) Harada, J. K.; Charles, N.; Poeppelmeier, K. R.; Rondinelli, J. M. Heteroanionic Materials by Design: Progress Toward Targeted Properties. *Adv. Mater.* **2019**, *31*, 1805295.

(18) Neuefeind, J.; Feygenson, M.; Carruth, J.; Hoffmann, R.; Chipley, K. K. The Nanoscale Ordered MAterials Diffractometer NOMAD at the Spallation Neutron Source SNS. *Nucl. Instrum. Methods Phys. Res. Sect. B Beam Interact. Mater. Atoms* **2012**, *287*, 68−75.

(19) Toby, B. H.; Von Dreele, R. B. It GSAS-II: The Genesis of a Modern Open-Source All Purpose Crystallography Software Package. *J. Appl. Crystallogr.* **2013**, *46*, 544−549.

(20) Coelho, A. A.; Chater, P. A.; Kern, A. Fast Synthesis and Refinement of the Atomic Pair Distribution Function. *J. Appl. Crystallogr.* **2015**, *48*, 869−875.

(21) Farrow, C. L.; Juhas, P.; Liu, J. W.; Bryndin, D.; Božin, E. S.; Bloch, J.; Proffen, T.; Billinge, S. J. L. PDFfit2 and PDFgui: Computer Programs for Studying Nanostructure in Crystals. *J. Phys.: Condens. Matter* **2007**, *19*, 335219.

(22) Kong, S.-T.; Deiseroth, H.-J.; Reiner, C.; Gün, Ö.; Neumann, E.; Ritter, C.; Zahn, D. Lithium Argyrodites with Phosphorus and Arsenic: Order and Disorder of Lithium Atoms, Crystal Chemistry, and Phase Transitions. *Chem. Eur J.* **2010**, *16*, 2198−2206.

(23) Perdew, J. P.; Burke, K.; Ernzerhof, M. Generalized Gradient Approximation Made Simple. *Phys. Rev. Lett.* **1996**, *77*, 3865−3868.
(24) Kresse, G.; Furthmüller, J. Efficient Iterative Schemes for Ab Initio Total-Energy Calculations Using a Plane-Wave Basis Set. *Phys. Rev. B: Condens. Matter Mater. Phys.* **1996**, *54*, 11169−11186.
(25) Blöchl, P. E. Projector Augmented-Wave Method. *Phys. Rev. B* **1994**, *50*, 17953−17979.
(26) Jain, A.; Ong, S. P.; Hautier, G.; Chen, W.; Richards, W. D.; Dacek, S.; Cholia, S.; Gunter, D.; Skinner, D.; Ceder, G.; Persson, K. A. Commentary: The Materials Project: A Materials Genome Approach to Accelerating Materials Innovation. *APL Mater.* **2013**, *1*, 011002.
(27) Ong, S. P.; Cholia, S.; Jain, A.; Brafman, M.; Gunter, D.; Ceder, G.; Persson, K. A. The Materials Application Programming Interface (API): A Simple, Flexible and Efficient API for Materials Data Based on REpresentational State Transfer (REST) Principles. *Comput. Mater. Sci.* **2015**, *97*, 209−215.
(28) Deng, Z.; Zhu, Z.; Chu, I.-H.; Ong, S. P. Data-Driven First-Principles Methods for the Study and Design of Alkali Superionic Conductors. *Chem. Mater.* **2017**, *29*, 281−288.
(29) Ong, S. P.; Wang, L.; Kang, B.; Ceder, G. Li−Fe−P−O_2 Phase Diagram from First Principles Calculations. *Chem. Mater.* **2008**, *20*, 1798−1807.
(30) Zhu, Y.; He, X.; Mo, Y. First Principles Study on Electrochemical and Chemical Stability of Solid Electrolyte−Electrode Interfaces in All-Solid-State Li-Ion Batteries. *J. Mater. Chem. A* **2016**, *4*, 3253−3266.
(31) Zhu, Z.; Chu, I.-H.; Ong, S. P. $Li_3Y(PS_4)_2$ and $Li_5PS_4Cl_2$: New Lithium Superionic Conductors Predicted from Silver Thiophosphates Using Efficiently Tiered Ab Initio Molecular Dynamics Simulations. *Chem. Mater.* **2017**, *29*, 2474−2484.
(32) Lacivita, V.; Westover, A. S.; Kercher, A.; Phillip, N. D.; Yang, G.; Veith, G.; Ceder, G.; Dudney, N. J. Resolving the Amorphous Structure of Lithium Phosphorus Oxynitride (Lipon). *J. Am. Chem. Soc.* **2018**, *140*, 11029−11038.
(33) Gautam, A.; Sadowski, M.; Ghidiu, M.; Minafra, N.; Senyshyn, A.; Albe, K.; Zeier, W. G. Engineering the Site-Disorder and Lithium Distribution in the Lithium Superionic Argyrodite Li_6PS_5Br. *Adv. Energy Mater.* **2020**, 2003369.
(34) Wang, P.; Liu, H.; Patel, S.; Feng, X.; Chien, P.-H.; Wang, Y.; Hu, Y.-Y. Fast Ion Conduction and Its Origin in $Li_{6-x}PS_{5-x}Br_{1+x}$. *Chem. Mater.* **2020**, *32*, 3833−3840.
(35) Hanghofer, I.; Brinek, M.; Eisbacher, S. L.; Bitschnau, B.; Volck, M.; Hennige, V.; Hanzu, I.; Rettenwander, D.; Wilkening, H. M. R. Substitutional Disorder: Structure and Ion Dynamics of the Argyrodites Li_6PS_5Cl, Li_6PS_5Br and Li_6PS_5I. *Phys. Chem. Chem. Phys.* **2019**, *21*, 8489−8507.
(36) Bloembergen, N.; Purcell, E. M.; Pound, R. V. Relaxation Effects in Nuclear Magnetic Resonance Absorption. *Phys. Rev.* **1948**, *73*, 679−712.
(37) Ganapathy, S.; Yu, C.; van Eck, E. R. H.; Wagemaker, M. Peeking across Grain Boundaries in a Solid-State Ionic Conductor. *ACS Energy Lett.* **2019**, *4*, 1092−1097.
(38) Gao, Y.; Nolan, A. M.; Du, P.; Wu, Y.; Yang, C.; Chen, Q.; Mo, Y.; Bo, S.-H. Classical and Emerging Characterization Techniques for Investigation of Ion Transport Mechanisms in Crystalline Fast Ionic Conductors. *Chem. Rev.* **2020**, *120*, 5954−6008.
(39) Bernges, T.; Culver, S. P.; Minafra, N.; Koerver, R.; Zeier, W. G. Competing Structural Influences in the Li Superionic Conducting Argyrodites $Li_6PS_{5-x}Se_xBr$ ($0 \leq x \leq 1$) upon Se Substitution. *Inorg. Chem.* **2018**, *57*, 13920−13928.

https://dx.doi.org/10.1021/acs.chemmater.0c04650
Chem. Mater. 2021, 33, 1435−1443